International Journal of Nanomedicine

Dovepress
Taylor & Francis Group

Open Access Full Text Article

ORIGINAL RESEARCH

Nanoengineered Macrophages for in vivo Three-Dimensional Photoacoustic Imaging and Immunotherapy of Acute Lung Injury

Yibo Tang[1,*], Chaohao Liang[1,*], Fan Meng[1,2,*], Wenjie Yin[1], Fengbing He[1], Jian Zhang[1]

[1]School of Biomedical Engineering, The First Affiliated Hospital of Guangzhou Medical University, Guangzhou Medical University, Guangzhou, Guangdong, People's Republic of China; [2]College of Biomedical Engineering & Instrument Science, Zhejiang University, Hangzhou, Zhejiang, People's Republic of China

*These authors contributed equally to this work

Correspondence: Jian Zhang, School of Biomedical Engineering, The First Affiliated Hospital of Guangzhou Medical University, Guangzhou Medical University, 1 Xinzhao Road, Xinzhao Town, Panyu District, Guangzhou, Guangdong, People's Republic of China, Email jianzhang@gzhmu.edu.cn

---

Background: Acute lung injury (ALI) is a life-threatening condition lacking effective real-time monitoring and targeted therapeutic strategies. Cell-based drug delivery systems offer promise but are limited by the inability to track their in vivo distribution and therapeutic response.

Methods: Macrophages were engineered to carry aluminum hydroxide-stabilized Tocilizumab (Alum/Toc) and labeled with indocyanine green (ICG) for photoacoustic (PA) imaging. The resulting platform (MΦ/ICG@Alum/Toc) was intravenously administered to Lipopolysaccharides (LPS)-induced ALI mice. Photoacoustic computed tomography (PACT) was used to monitor the dynamic recruitment, pulmonary accumulation, and clearance of the engineered cells over 48 h. Therapeutic efficacy was evaluated by histopathology and lung wet/dry ratio, and biosafety was assessed in major organs.

Results: PACT enabled non-invasive, high-resolution tracking of nanoengineered macrophages, revealing rapid homing to inflamed lungs within 6 h, peak accumulation at 24 h, and subsequent hepatic clearance. Three-dimensional (3D) volumetric analysis confirmed targeted pulmonary delivery with minimal off-target distribution. The MΦ/ICG@Alum/Toc platform significantly reduced alveolar edema, inflammatory infiltration, and histopathological scores compared to free Toc, demonstrating superior therapeutic efficacy with excellent biocompatibility.

Conclusion: This study establishes PACT as a powerful tool for guiding and monitoring cell-based therapies in real time. The nanoengineered macrophage platform offers a clinically translatable strategy for precision immunotherapy of ALI, with potential applications in other inflammatory diseases.

Keywords: nanoengineered macrophages, photoacoustic imaging, acute lung injury, targeted drug delivery, theranostics

---

Introduction

Acute Lung Injury (ALI) and Acute Respiratory Distress Syndrome (ARDS) represent life-threatening respiratory failures characterized by rapid-onset pulmonary inflammation, impaired gas exchange, and progressive hypoxemia.[1–3] The uncontrolled inflammatory storm associated with ALI/ARDS frequently causes multiple organ dysfunction syndrome, leading to a mortality rate of 20~40%.[3,4] The pathogenesis of ALI is mainly due to the hyperactivation of alveolar macrophages, which triggers a destructive "cytokine storm" through excessive release of pro-inflammatory factors and chemokines.[5–7] This inflammatory cascade not only directly damages tissues, but also recruits circulating macrophages and neutrophils into pulmonary tissues, eliciting a sustained vicious cycle in inflammatory microenvironment. Current clinical management remains largely supportive, relying on mechanical ventilation and adjunctive anti-inflammatory therapies, underscoring the urgent need for targeted therapeutic strategies with real-time monitoring capabilities.[8–10]

https://doi.org/10.2147/IJN.S608394
Received: 17 March 2026
Accepted: 2 June 2026
Published: 10 June 2026

Despite the widespread use of conventional clinical imaging techniques such as chest X-ray, computed tomography (CT), lung ultrasound (LUS) and magnetic resonance imaging (MRI) for diagnosing ALI/ARDS,[11–13] the presence of numerous limitations remains a concern. For instance, conventional X-ray provides only two-dimensional projections with limited tissue differentiation, while CT and X-ray involve ionizing radiation that raises safety concerns for repeated examinations.[13–15] Moreover, pulmonary MRI suffers from suboptimal image quality due to the low proton density of lung parenchyma, coupled with high costs and technical constraints that limit its widespread application.[16,17] Collectively, these imaging modalities demonstrate low sensitivity and specificity in distinguishing acute inflammatory processes from other pulmonary pathologies, thereby impeding precise diagnosis of ALI. Therefore, it is urgent to explore an imaging approach that is free of ionizing radiation and non-invasive, while combining both imaging depth and precision, for the early diagnosis and interventional treatment of ALI.

Photoacoustic imaging (PAI) leverages the photoacoustic (PA) effect, in which pulsed laser-induced thermoelastic expansion generates ultrasonic waves, thereby combining the high contrast of optical imaging with the deep penetration of ultrasound to overcome the depth limitations of conventional optical microscopy.[18–22] Photoacoustic computed tomography (PACT), as a principal implementation of PAI, utilizes multi-element transducer arrays and nanosecond pulsed lasers with tunable wavelengths to achieve deep-tissue penetration, while maintaining high spatial resolution.[23–26] This technique supports multi-parametric functional imaging and has demonstrated utility in tumor vasculature mapping, neurovascular monitoring, cardiovascular assessment, vaccine tracking, and immune cell tracking within lymphatic networks.[27–32] However, PACT applications have been predominantly applied in tumor diagnosis, while their utilization in visualizing deep-seated organs and tissues remains limited due to constraints in penetration depth and spatial resolution.[14,33–35] Despite development of targeted nanomaterials to improve specificity, their efficacy in pulmonary imaging remains limited by inadequate accumulation at target sites, rapid clearance, and severe acoustic attenuation at air-tissue interfaces compounded by respiratory motion artifacts.[36] These obstacles necessitate the development of engineered nanocarriers with optimized pulmonary biodistribution and specific affinity for inflammatory biomarkers.

Macrophage-mediated drug delivery, capitalizing on the innate inflammatory tropism of macrophages, has emerged as a promising strategy for targeted ALI therapy.[37–41] However, the therapeutic efficacy of this strategy is often compromised by the natural exocytosis of carrier cells, which leads to premature drug loss during systemic circulation.[42,43] To address premature drug release during systemic circulation, various nanoparticulate systems have been engineered to encapsulate therapeutic agents and prevent exocytosis from carrier cells, thereby enhancing drug bioavailability.[38] For instance, nanoparticles modified with host–guest molecules have been designed to form intracellular aggregates within macrophages, thereby resisting premature systemic release.[39] Similarly, aluminum hydroxide adjuvant (Alum), a naturally occurring nanoparticulate aggregate widely used in vaccines, can stabilize soluble therapeutics into forms less prone to exocytosis, positioning it as a promising platform for enhanced targeted drug delivery.[44–46] Tocilizumab (Toc), a recombinant humanized monoclonal antibody that blocks interleukin-6 (IL-6) signaling, is clinically approved for rheumatoid arthritis and has demonstrated therapeutic potential in severe inflammatory pneumonia during the COVID-19 pandemic.[47,48] To enhance the targeted delivery efficiency of Toc, we developed a nanoengineered live-cell platform by loading macrophages with Alum nanoparticles that stabilize Toc, forming MΦ@Alum/Toc nanocomplexes. These nanoengineered macrophage carriers (MΦ/ICG@Alum/Toc) were labeled with indocyanine green (ICG) for PAI and integrated with a custom-built PACT system to establish a precise theranostic platform for ALI, enabling simultaneous diagnosis and therapy (Scheme 1).

Using PACT, we achieved non-invasive tracking of nanoengineered macrophages, revealing rapid homing to inflamed lungs (6 h) with peak accumulation at 24 h. Three-dimensional (3D) analysis confirmed targeted pulmonary delivery with minimal off-target distribution. Compared to free Toc, the MΦ/ICG@Alum/Toc platform significantly reduced alveolar edema, inflammatory infiltration, and histopathological scores, demonstrating superior therapeutic efficacy and biocompatibility. This integrated approach establishes PACT as a vital tool for guiding cell-based nanotherapies in inflammatory lung diseases.

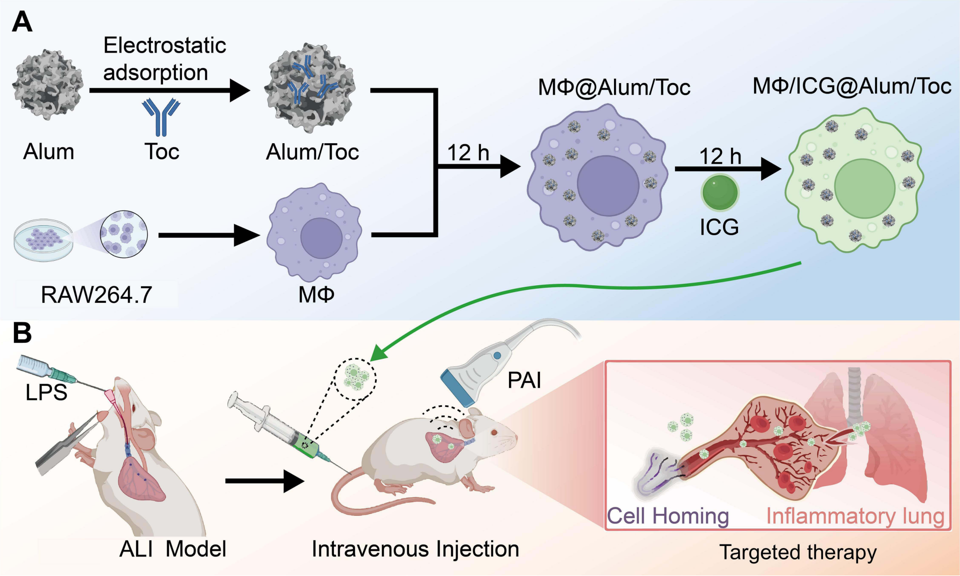

Scheme 1 Schematic diagram of the engineered macrophage delivery system. (**A**) The engineered macrophage carrier MΦ/ICG@Alum/Toc was fabricated through a multi-step procedure involving the electrostatic adsorption of Toc onto Alum, incubation with macrophages, and ICG labeling, thereby creating a system capable of anti-inflammatory drug delivery and PAI. (**B**) Driven by cellular homing effects, the engineered macrophages rapidly targeted the lung inflammation sites after tail vein injection in an LPS-induced ALI mouse model, resulting in significant accumulation by 24 h. With the assistance of the PACT system, the aggregation process of these live cellular carriers could be monitored in real time.

Materials and Methods

Materials

Toc was purchased from Beijing Solarbio Science & Technology Co., Ltd. Aluminum hydroxide adjuvant (Alum) was purchased from Invitrogen, USA. indocyanine green (ICG) and hematoxylin and eosin (H&E) staining solutions were purchased from Shanghai Yuanye Biotechnology Co., Ltd. Bicinchoninic Acid Assay (BCA) protein assay kit was purchased from Shanghai Maclean Biotechnology Co., Ltd. Cell Counting Kit-8 (CCK-8) kit was purchased from Merck, Germany. Lipopolysaccharides (LPS) and Lumogallion (LG) were purchased from Beyotime Biotechnology Co., Ltd. Anti-F4/80 and anti-MPO monoclonal antibodies were obtained from Abcam Trading (Shanghai) Co., Ltd. The 3,3′-diaminobenzidine (DAB) substrate kit was purchased from Fuzhou Maixin Biotech, Ltd. Enzyme-linked immunosorbent assay (ELISA) kits for mouse cytokines were sourced from Wuhan Boster Biological Technology Co., Ltd. RAW264.7 cells were obtained from the American Type Culture Collection (ATCC, TIB-71™, Manassas, VA, USA).

Preparation of Engineered Macrophage Carriers

Toc was adsorbed onto Alum via electrostatic interaction by incubating 20 µg of positively charged Toc with 40 µg of negatively charged Alum at room temperature for 30 min to form Alum/Toc complexes. Free Toc was removed by centrifugation. The adsorption effect of Alum on Toc was tested by measuring the free protein concentration in the supernatant using a BCA protein assay kit. Subsequently, RAW264.7 murine macrophages were cultured overnight to 70–80% confluence and then incubated with Alum/Toc for 12 h to enable cellular uptake, resulting in engineered macrophages (MΦ@Alum/Toc). The cells were then labeled by incubation with ICG (1 mg/mL) under light-protected conditions at room temperature. Following thorough washing with serum-free medium to remove unbound dye, the final engineered macrophage carrier MΦ/ICG@Alum/Toc was obtained for subsequent PAI.

PACT System

The PACT system was constructed using a MarsonicsDAQ PA data acquisition unit (Beijing Tsingpai Technology Co., China) as its core component. This advanced data acquisition system supports 128 parallel channels with a maximum sampling rate of 40 MHz to ensure high-fidelity signal capture. PA signals were generated by a tunable nanosecond pulsed laser system

(Continuum, USA) that produces fundamental outputs at both 532 and 1064 nm wavelengths. Through precise optical parametric oscillator tuning, the laser output could be continuously adjusted across the spectral range of 680–940 nm, generating light pulses with durations of 5–10 ns and pulse energies of 25 mJ. The laser output beam was first focused using a customized convex lens (Daheng New Epoch Technology Inc., China) to optimize coupling efficiency into a fiber (Beijing Tsingpai Technology Co., China). This optical arrangement produced uniform rectangular illumination on the tissue surface with consistent energy distribution. A customized 128-element linear transducer array (Beijing Tsingpai Technology Co., China) was applied for PA signal detection. This transducer array featured a center frequency of 7.5 MHz with 60% bandwidth and an element pitch of 0.03 cm. During imaging operations, the laser repetition rate was maintained at 20 Hz, which enabled real-time PAI at frame rates up to 20 frames per second, sufficient for capturing dynamic physiological processes. Both raw and reconstructed data were saved simultaneously during scanning. To improve image quality, radiofrequency (RF) data were independently reconstructed using MATLAB. To obtain the 3D distribution of adjuvants within organs, the laser repetition frequency was maintained at 20 Hz, and combined with the slow movement of the motor slide, tomographic scan slices with an interval of 0.08 mm were generated for 3D reconstruction. The obtained slices were reconstructed on the y-axis to obtain PA 3D results.

Characterization

The morphology of Alum/Toc was evaluated using transmission electron microscopy (TEM) (Talos F200S, Thermo Fisher Scientific, America). The hydrodynamic particle size distribution and electrical potentials of Alum, Toc, and Alum/Toc were determined using a Zetasizer instrument (ZETASIZER NANO ZS, Malvern, England). The phagocytosis of Alum/Toc@LG by macrophages at different time points was monitored using fluorescence microscopy (Ti2-E, Nikon, Japan) and quantitatively analyzed by flow cytometry. Finally, the absorption spectra of ICG, MΦ@Alum/Toc, and MΦ/ICG@Alum/Toc were measured using UV-Vis absorption spectroscopy (UV-2600, SHIMADZU, Japan).

The in vitro PAI performance of MΦ/ICG@Alum/Toc was systematically evaluated. First, MΦ/ICG@Alum/Toc was injected into transparent plastic tubing, and continuous scanning was performed in 10 nm steps within the range of 680 nm to 900 nm, acquiring signal intensity at each wavelength. Next, the relationship between PA signal and concentration was tested. MΦ/ICG@Alum/Toc samples with different cell masses were injected into transparent plastic tubing, and PA scanning imaging was performed at a 770 nm laser excitation wavelength to acquire cross-sectional PA images corresponding to each concentration, followed by quantitative analysis of the PA signal intensity. Finally, the stability of the PA signal was evaluated by continuously irradiating the samples at the laser wavelength for 20 min. During this process, the system continuously acquired PA signals and extracted a one-dimensional signal intensity curve over time.

PACT System Parameters

The axial resolution and imaging width of the system were measured using a 50 μm-diameter copper wire. A tissue-mimicking phantom composed of agar and milk was constructed to simulate the optical absorption and scattering properties of human tissues. 3D reconstruction in the X-Z plane was performed using uniformly dispersed copper wire fragments within the phantom, to obtain the imaging depth of the system.

Cytotoxicity

To evaluate the cytotoxicity of ICG@Alum/Toc against RAW264.7 macrophages, cell viability was determined using the CCK-8 assay. RAW264.7 cells were seeded at a density of 5×10^3 cells/well in 96-well plates and cultured for 24 h. Different concentrations of ICG@Alum/Toc were then added and incubated for another 24 h. After incubation, 10 μL of CCK-8 solution was added to each well, and the plates were incubated in the dark for 2 h. The absorbance at 450 nm was read using a microplate reader, and cell viability was calculated.

Animal Model and in vivo Imaging

Animal experiments were conducted using male BALB/c mice (6–8 weeks old) supplied by Guangdong Zhiyuan Biomedical Technology Co., Ltd. All animals were housed in a specific pathogen-free facility with unrestricted access to water and a standard diet. To induce the ALI model, mice were anesthetized with an intraperitoneal injection of 1%

sodium pentobarbital (35–40 mg/kg), with anesthetic depth confirmed by the absence of a pedal reflex, followed by intratracheal administration of LPS (8 mg/kg).

For in vivo imaging studies, ALI mice were intravenously administered the MΦ/ICG@Alum/Toc cell suspension. During PACT imaging, animals were maintained under anesthesia with 1.5–2% isoflurane and continuously physiologically monitored. Pulmonary and hepatic images were acquired at 0, 1, 2, 12, 24, and 48 h post-injection. To complement the PACT findings, in vivo fluorescence imaging was performed using an IVIS imaging system (PerkinElmer, USA) at the same time points after intravenous injection of LG-labeled MΦ/ICG@Alum/Toc. At the experimental endpoint, mice were humanely euthanized by cervical dislocation, and death was confirmed by the cessation of heartbeat and respiration prior to tissue collection. The harvested lungs and liver were sectioned (10 μm) and observed under a fluorescence microscope (ZEISS 900, Germany) to assess the distribution of LG-labeled nanoparticles.

Therapeutic Efficacy and Biosafety

After 48 h of imaging, mice were euthanized, and lung tissue were harvested immediately from each mouse. A portion of lung tissue was weighed (wet weight), dried at 60 °C for 48 h to a constant weight (dry weight), and the wet/dry weight ratio was calculated to assess pulmonary edema. The remaining lung tissue was fixed with 4% paraformaldehyde. The fixed lung tissue was dehydrated, embedded, sectioned, stained with H&E staining solution, and images were acquired using a digital pathology scanner (Olympus CX31, Japan). Pathological scoring was performed on the sections. To assess inflammatory cell infiltration within the alveoli, immunohistochemistry (IHC) was performed for the macrophage marker F4/80 and the neutrophil marker myeloperoxidase (MPO). Lung sections were processed for antigen retrieval, blocked, and incubated with primary antibodies (F4/80 or MPO) followed by HRP-conjugated secondary antibody. Antigen-antibody complexes were visualized using a DAB substrate kit, followed by counterstaining with hematoxylin. Images were captured with a digital pathology scanner, and the percentages of F4/80- or MPO-positive areas were quantified using ImageJ software.

To evaluate anti-inflammatory and antioxidant efficacy, lung tissue homogenates were prepared. Levels of pro-inflammatory cytokines (TNF-α, IL-6, IL-1β) were quantified using commercial ELISA kits, and malondialdehyde (MDA) as well as total superoxide dismutase (T-SOD) levels were measured using corresponding assay kits (Servicebio), all according to the manufacturers' instructions. Total protein concentration was determined using a BCA protein assay kit for normalization.

To evaluate systemic inflammatory responses, blood samples were collected and analyzed using an automated hematology analyzer (BC-5000vet, Mindray, China) to determine white blood cell (WBC), red blood cell (RBC), platelet (PLT), and lymphocyte (Lymph) counts. For biosafety assessment, PBS, free Toc, or MΦ@Alum/Toc was intravenously injected into healthy mice. After seven days, the mice were euthanized, and the heart, liver, spleen, and kidneys were harvested for H&E staining.

Statistical Analysis

All experiments were replicated at least three times. Data are expressed as mean ± SD. Statistical comparisons were conducted using Student's *t*-test or Multiple *t*-test (GraphPad Prism 9). Statistical significance is indicated as: $^*P < 0.05$, $^{**}P < 0.01$, $^{***}P < 0.001$, $^{****}P < 0.0001$; ns, not significant.

Results and Discussion

Characterization Results

TEM and quantitative size distribution analysis revealed well-dispersed nanoparticles with sizes ranging from 400 to 600 nm (Figure 1A and B), indicating successful complex formation. Hydrodynamic characterization showed that Alum/Toc particles in aqueous solution exhibited a predominant diameter of approximately 600 nm (Figure S1A, Supplementary Material) and a nearly neutral surface potential (Figure 1C), properties that facilitate efficient cellular internalization. The Alum/Toc complex demonstrated robust stability, as the adsorption efficiency remained close to 100% at all examined

https://doi.org/10.2147/IJN.S608394

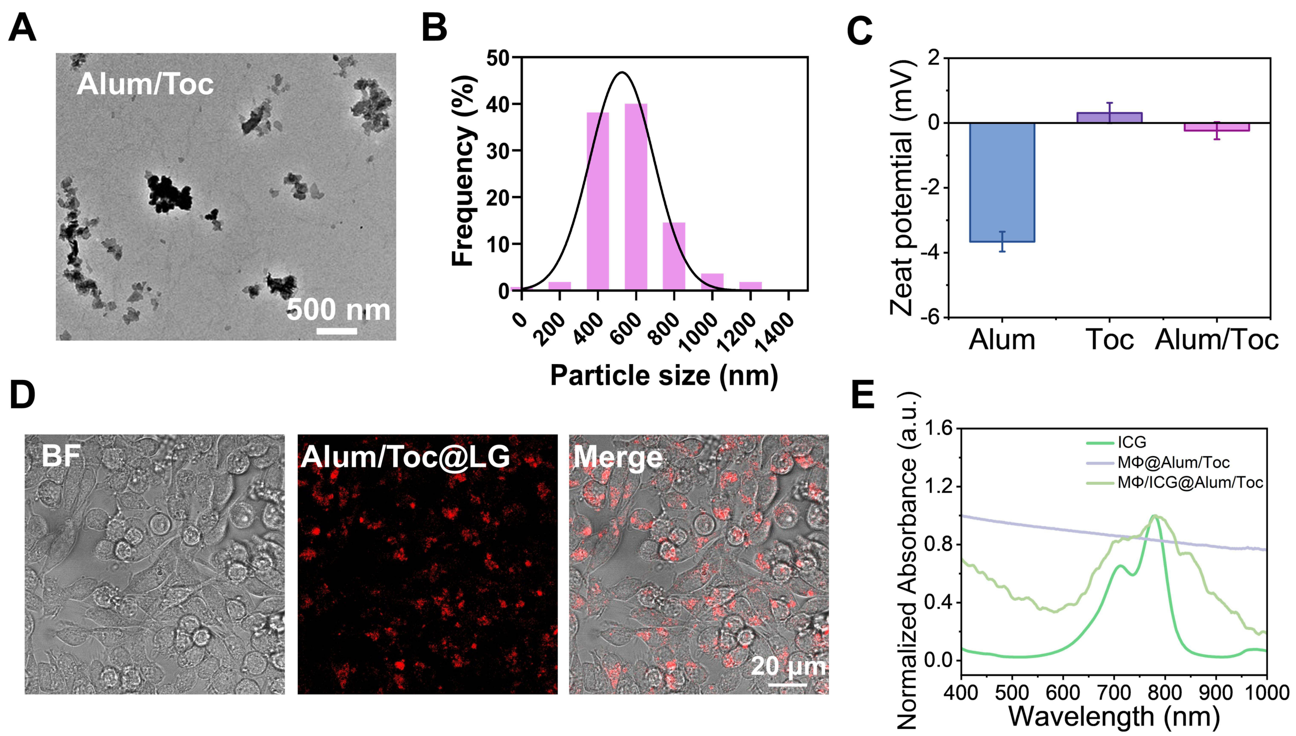

Figure 1 The characterization of MΦ/ICG@Alum/Toc. (**A**) TEM images of Alum/Toc. (**B**) Size distribution of Alum/Toc nanoparticles determined from 100 randomly selected particles in TEM images. (**C**) Zeta potential of Alum, Toc, and Alum/Toc. (**D**) Fluorescence imaging of Alum/Toc@LG engulfed by macrophages for 12 h. (**E**) UV absorption spectra of ICG, MΦ@Alum/Toc and MΦ/ICG@Alum/Toc.

time points (0, 2, 4, 8, 24, and 48 h) (Figure S1B, Supplementary Material). To visualize intracellular distribution, Alum/Toc was fluorescently labeled with LG (Alum/Toc@LG). Fluorescence microscopy confirmed efficient phagocytosis by RAW264.7 macrophages after 12 h of incubation (Figure 1D). Quantitative flow cytometry analysis further revealed time-dependent increase in uptake efficiency, reaching a peak of 29% at 12 h, followed by a slight decline at 24 h likely due to partial exocytosis (Figure S1C, Supplementary Material). Optical characterization revealed that MΦ/ICG@Alum/Toc exhibited a UV-vis absorption profile closely matching that of free ICG, with a characteristic peak near 780 nm (Figure 1E), confirming its suitability for near-infrared optical imaging.

PA Performance Characterization

The PACT system has a resolution of up to 85 μm (Figure S2A and B, Supplementary Material), while also having an imaging width of 4 cm (Figure S2C, Supplementary Material) and an imaging depth of 3 cm (Figure S2D, Supplementary Material). The PA signal of MΦ/ICG@Alum/Toc exhibits significantly different intensity distributions in the 680–800 nm range (Figure 2A), with a maximum at 770 nm, consistent with its UV absorption characteristics. This spectral discrepancy is attributed to variations in spectroscopic and photophysical behavior, supporting the selection of 770 nm for in vivo PAI. The PA signal intensity exhibited a linear correlation with cell concentration (Figure 2B) and remained stable under prolonged laser irradiation (Figure 2C), confirming the robustness of MΦ/ICG@Alum/Toc for tracking macrophage migration in living animals.

PA Images of MΦ/ICG@Alum/Toc in vivo

The PACT system consists of multiple parts and obtains 3D reconstruction results by reconstructing along the y-axis (Figure S3, Supplementary Material). To evaluate the in vivo targeting and imaging potential of MΦ/ICG@Alum/Toc in pneumonic regions, the construct was intravenously administered to LPS-induced ALI mice, followed by real-time pulmonary and hepatic imaging using a PACT system. A control group injected with free ICG dye was included for comparison. Mice receiving free ICG exhibited negligible pulmonary accumulation throughout the 48-h observation period (Figure 3A). In contrast, strong ICG signals

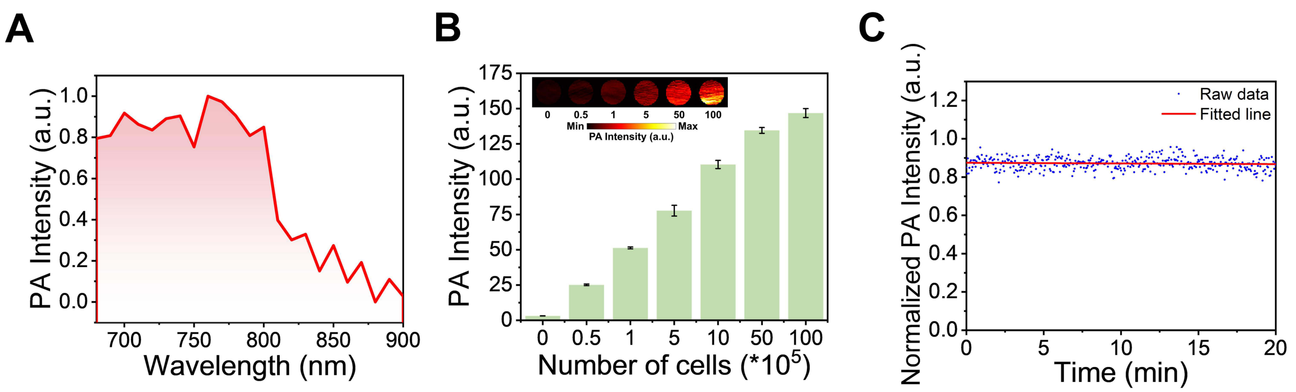

Figure 2 The PA performance characterization of MΦ/ICG@Alum/Toc. (**A**) PA signal intensity of MΦ/ICG@Alum/Toc at different wavelengths. (**B**) PA images and intensity of MΦ/ICG@Alum/Toc with different numbers of cells. (**C**) Stability of MΦ/ICG@Alum/Toc under PA conditions for 20 min.

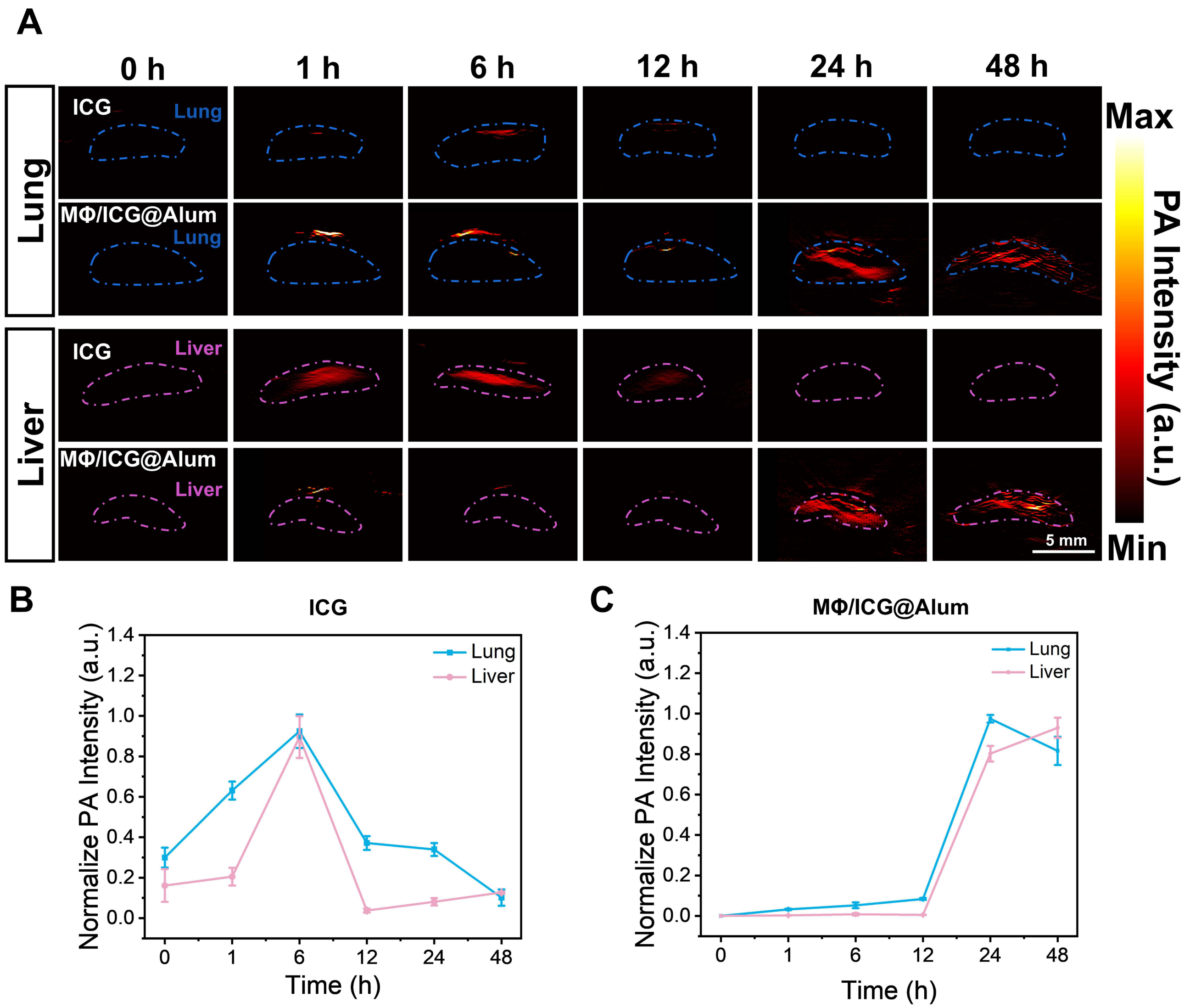

Figure 3 PA images of mice after intravenous injection of MΦ/ICG@Alum/Toc. (**A**) PA images of the lung and liver of ICG and MΦ/ICG@Alum/Toc injected at different times (0, 1, 6, 12, 24, and 48 h). (**B**) Normalized PA signal intensity in the lung and liver after ICG injection. (**C**) Normalized PA signal intensity in the lung and liver after MΦ/ICG@Alum/Toc injection.

https://doi.org/10.2147/IJN.S608394

were detected in the liver as early as 1 h, intensified by 6 h, and gradually declined after 12 h, reflecting rapid hepatic metabolism and clearance of free ICG. Quantitative PA signal analysis further illustrated this process (Figure 3B).

In pneumonia mice administered with MΦ/ICG@Alum/Toc, significant PA signals emerged in peripulmonary vasculature at 1 h, suggesting that the circulating engineered macrophages rapidly homed to inflammatory lung vessels. By 6 h, vascular signals diminished while pulmonary signals appeared, indicating migration of the carrier from vasculature into alveolar spaces. At 12 h, vascular signals nearly disappeared, and lung signals continued to increase, peaking at 24 h and beginning to decline by 48 h. In the liver, minimal ICG signal was observed during 1–12 h, indicating negligible off-target accumulation. The hepatic signal detected at 24 h and its increase by 48 h reflect the gradual clearance and metabolism of ICG-labeled nanomaterials from the liver.

Quantitative PA intensity analysis confirmed significant pulmonary accumulation at 12 h (Figure 3C), with signal intensity increasing more than six-fold by 24 h and remaining over five-fold higher than the 12 h level at 48 h. In the liver, a notable ICG signal emerged at 24 h and rose approximately 1.2-fold by 48 h. These results demonstrate that MΦ/ICG@Alum/Toc enables specific targeting to pneumonic areas, supporting its viability as a drug delivery system with efficient distribution, organ-specific accumulation, and controlled metabolic clearance.

To complement the PACT findings, we performed additional in vivo fluorescence imaging and ex vivo fluorescence sectioning of the lungs and liver. ALI mice were intravenously injected with LG-labeled MΦ/ICG@Alum/Toc. Fluorescence signals progressively accumulated in the thoracic region from 2 h onward and persisted through 48 h, while abdominal signals increased after 12 h and peaked at 48 h, indicating hepatic clearance (Figure S4, Supplementary Material). Fluorescence microscopy of tissue sections (Figure S5A and B, Supplementary Material) showed moderate green fluorescence in the lungs at 12 h, which remained robust at 24 h and substantial at 48 h. Liver fluorescence was weak at 12 h, increased notably at 24 h, and peaked at 48 h. The ex vivo results are fully consistent with the PACT data, confirming that engineered macrophages accumulate in inflamed lungs by 12 h, persist beyond 48 h, and are cleared via the liver.

3D PA Images of MΦ/ICG@Alum/Toc in vivo

3D PAI enabled non-invasive tracking of the temporal and spatial distribution of MΦ/ICG@Alum/Toc in living mice. The reconstructed images revealed initial pulmonary accumulation at 12 h post-injection, which expanded significantly by 24 h and subsequently decreased by 48 h (Figure 4A). Quantitative analysis at 24 h post-injection revealed peak distribution in both lungs and liver, with lung volumetric and surface area measurements of 251.36 mm^3 and 3360.97 mm^2, and liver measurements of 139.03 mm^3 and 1849.49 mm^2, respectively (Figure 4B and C). By 48 h, hepatic metrics increased to 361.11 mm^3 and 4359.92 mm^2, while pulmonary values declined to 136.73 mm^3 and 2270.24 mm^2. These spatiotemporal changes reflect a dynamic physiological process: the initial pulmonary accumulation demonstrates the carrier's ability to target inflamed lung tissue via cellular homing, while the subsequent signal shift indicates clearance through the mononuclear phagocyte system and eventual hepatic processing. The significantly higher aluminum levels detected in lung tissues than those in liver tissues at 12 h, as summarized in Figure 4D, further corroborate the targeted pulmonary delivery. This distinct biodistribution enables high-contrast imaging of pulmonary inflammatory sites with improved spatial precision.

Evaluation of MΦ@Alum/Toc Treatment in ALI Mice

The therapeutic effect of MΦ@Alum/Toc was systematically evaluated in an LPS-induced murine model of ALI. Gross morphological examination (Figure S6A, Supplementary Material) and histopathological examination of H&E-stained lung sections (Figure 5A) revealed that LPS caused severe pulmonary hyperemia, edema, alveolar wall thickening, and inflammatory cell infiltration. Treatment with MΦ@Alum/Toc markedly alleviated these pathological changes, restoring lung morphology to near-healthy levels. To further evaluate the immunotherapeutic efficacy of the nanoplatform, we performed IHC staining, which revealed that LPS challenge significantly increased the alveolar infiltration of macrophages (F4/80-positive) and neutrophils (MPO-positive). Notably, this massive cellular infiltration was markedly alleviated following MΦ@Alum/Toc treatment (Figure 5B and C).

Consistent with the histological improvements, semi-quantitative histopathological scoring (Figure 5D) and wet/dry weight ratio analysis (Figure 5E) confirmed that MΦ@Alum/Toc significantly reduced lung injury scores and alleviated pulmonary edema compared to the PBS group. As shown in Figure 5F and G, quantitative analysis further revealed that LPS challenge

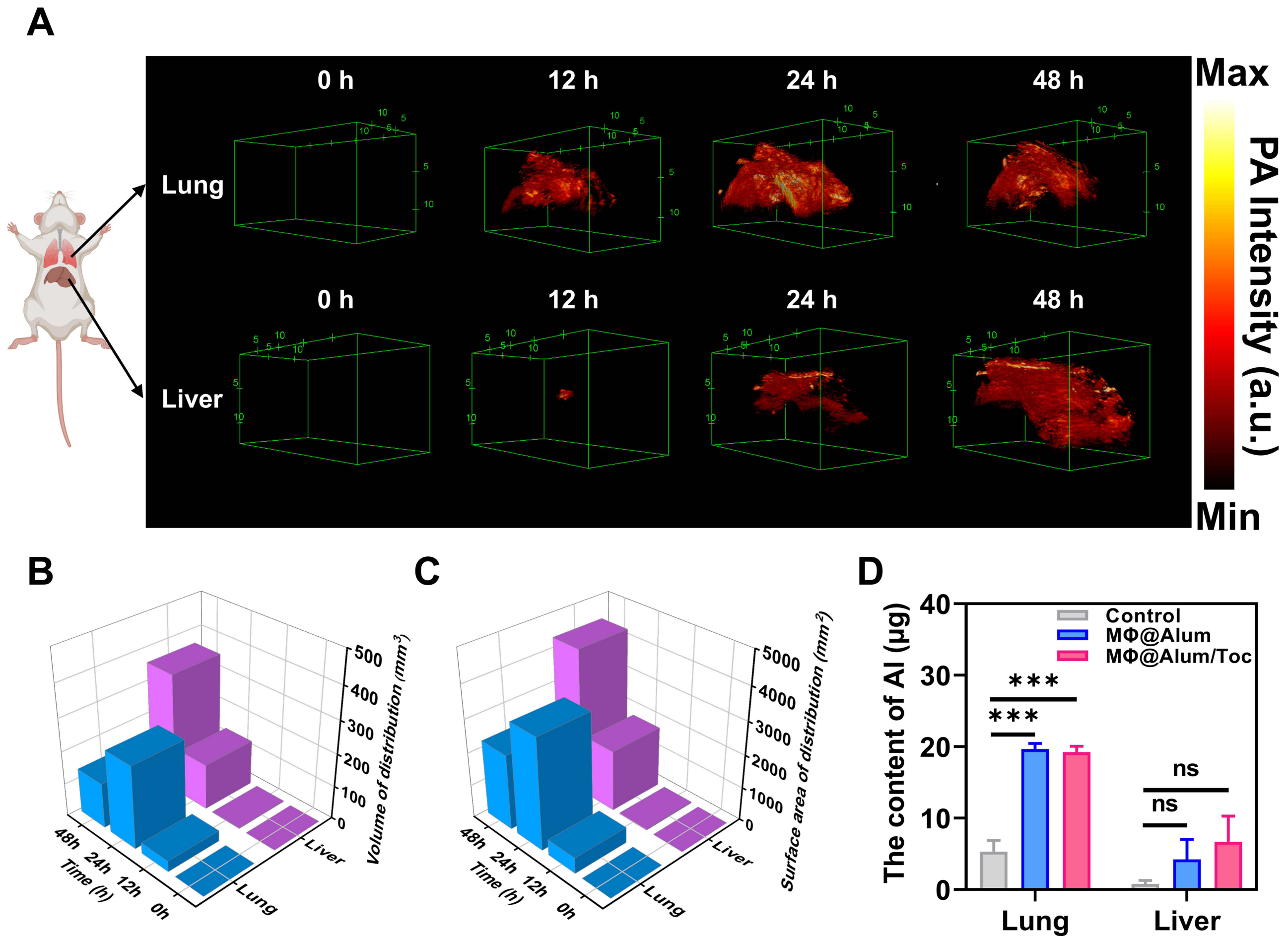

Figure 4 3D PA images of MΦ/ICG@Alum/Toc in the lung and liver in vivo. (**A**) 3D PA images of the lung and liver at different times (0, 12, 24, and 48 h). (**B**) Quantitative analysis of the PA signal volumes in the lung and liver. (**C**) Quantitative analysis of the PA signal surface area in the lung and liver. (**D**) Levels of aluminum in the lungs and liver at 12 h. Data are presented as mean ± SD (n = 3). Statistical significance was determined using a Multiple *t*-test for comparisons multiple groups or multiple time points. $^{***}P < 0.001$.

Abbreviation: ns, not significant.

induced massive infiltration of macrophages (4.8%) and neutrophils (38.7%) in the lungs. Treatment with MΦ@Alum/Toc dramatically reduced both cell types to near-normal levels (macrophages ~0.2%, neutrophils ~2.9%), outperforming free Toc (macrophages ~2.7%, neutrophils ~13.2%). ELISA of lung homogenates (Figure S6B-D, Supplementary Material) showed that MΦ@Alum/Toc significantly decreased pro-inflammatory cytokines (IL-1β, $P < 0.001$; TNF-α, $P < 0.05$; IL-6, $P < 0.05$) relative to LPS group, while free Toc only lowered IL-1β and IL-6 but failed to suppress TNF-α. Moreover, LPS elevated MDA to ~1.5 nmol/mg (Figure 5H) and suppressed T-SOD to ~75 U/mg (Figure 5I), indicating oxidative stress. Free Toc showed no effect, whereas MΦ@Alum/Toc significantly reduced MDA (~1.3 nmol/mg, $P < 0.05$) and restored T-SOD (~100 U/mg, $P < 0.05$), indicating suppression of lipid peroxidation and recovery of antioxidant capacity (Figure 5H and I).

Collectively, these results demonstrate that macrophage-mediated targeted delivery of Toc enhances anti-inflammatory, antioxidant, and immunomodulatory efficacy, markedly reducing immune cell infiltration and cytokine storm, thereby outperforming free Toc alone.

Hematological Analysis and Biocompatibility

To assess systemic inflammatory responses, complete blood counts were measured. LPS challenge significantly reduced WBC and PLT counts ($P < 0.05$), reflecting leukocyte recruitment to inflamed lungs and coagulation dysfunction. Treatment with free Toc or MΦ@Alum/Toc restored WBC and PLT to normal levels, while RBC and Lymph counts

https://doi.org/10.2147/IJN.S608394

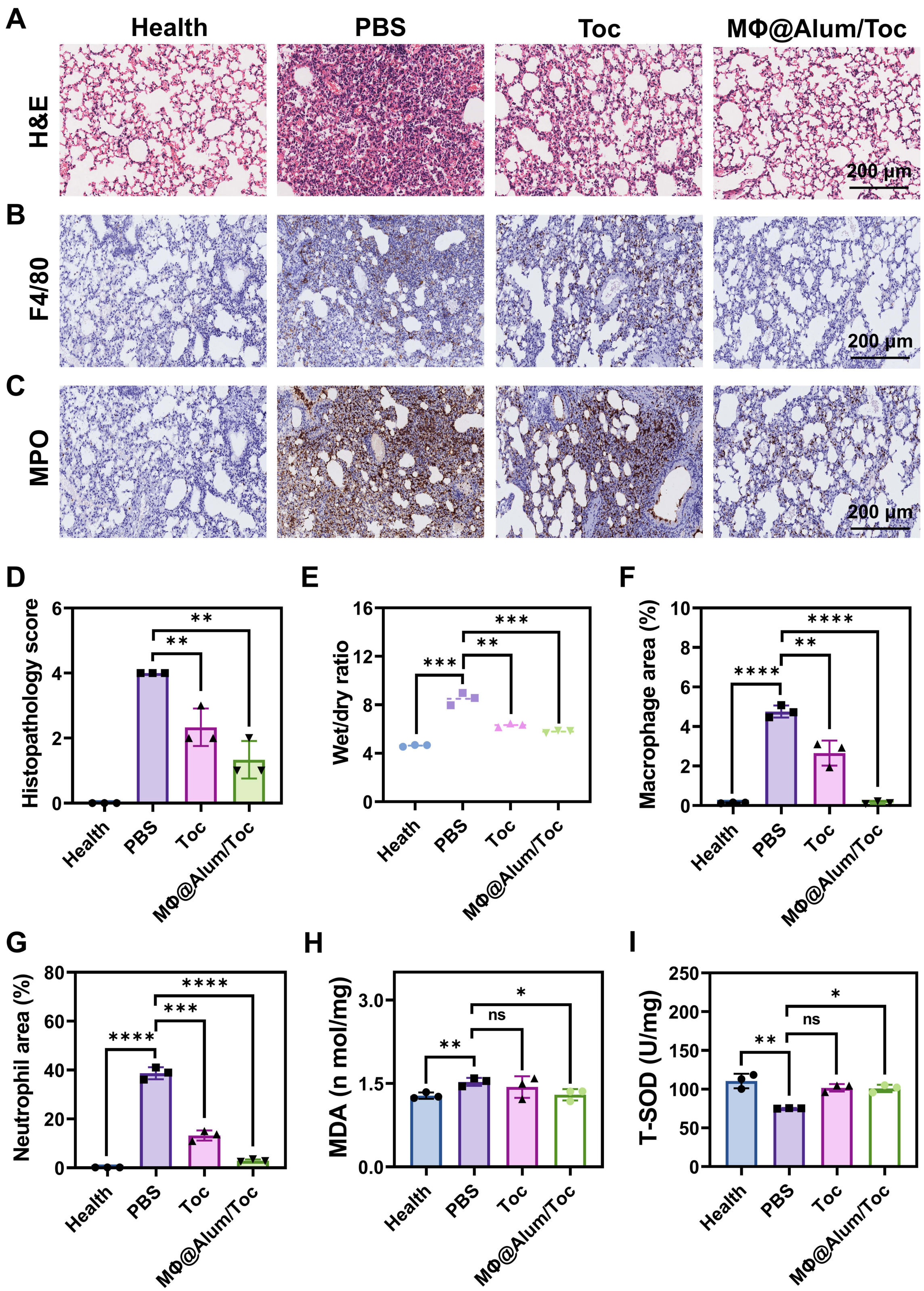

Figure 5 Assessment of MΦ@Alum/Toc therapeutic efficacy. (**A**) H&E-stained lung slice after treatment for 24 h. (**B**) IHC staining of lung sections for the macrophage marker F4/80. (**C**) IHC staining of lung sections for the neutrophil marker MPO. (**D**) Histopathology score of H&E-stained lung slice. (**E**) Wet/dry ratio of excised lungs after treatment for 24 h. (**F**) Quantitative analysis of F4/80-positive area percentages. (**G**) Quantitative analysis of MPO-positive area percentages. (**H**) Levels of MDA in lung tissue homogenates. (**I**) Levels of T-SOD in lung tissue homogenates. Data are presented as mean ± SD (n = 3). Statistical significance was determined using a two-tailed unpaired Student's *t*-test for comparisons between two groups. *$P < 0.05$, **$P < 0.01$, ***$P < 0.001$, ****$P < 0.0001$.

Abbreviation: ns, not significant.

https://doi.org/10.2147/IJN.S608394

remained unchanged across all groups (Figure 6A–D). The MΦ@Alum/Toc group showed values within normal reference ranges, confirming no systemic hematological toxicity.

The cytotoxicity of ICG@Alum/Toc against RAW264.7 macrophages was evaluated using the CCK-8 assay. As shown in Figure S7 (Supplementary Material), cell viability remained above 90% at concentrations up to 2.88 mg/mL, indicating negligible cytotoxicity. For in vivo biosafety assessment, healthy mice were intravenously injected with PBS, free Toc, or MΦ@Alum/Toc. After seven days, major organs (heart, liver, spleen, kidneys) were collected for H&E

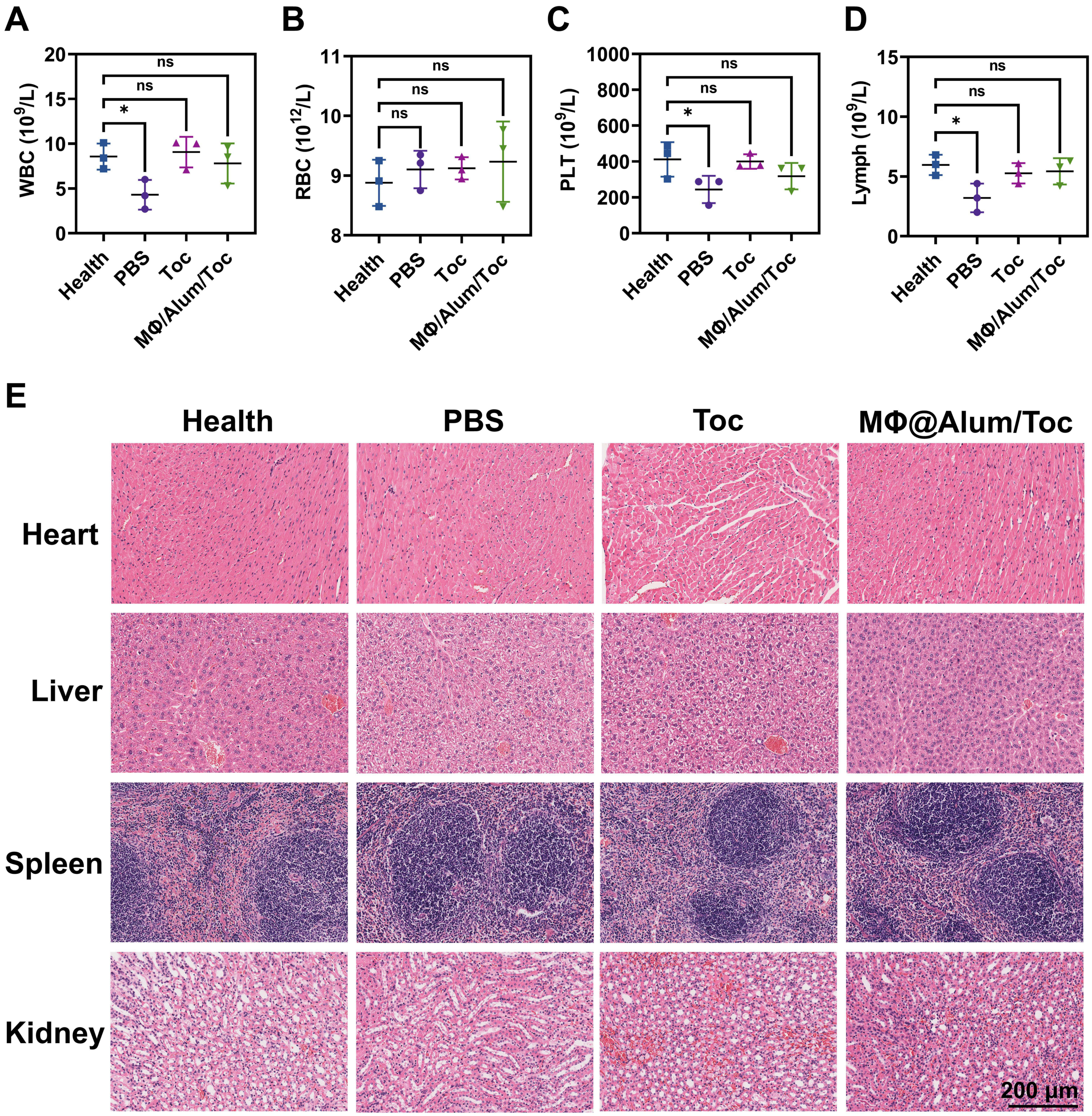

Figure 6 Hematological parameters and in vivo biosafety assessment. (**A-D**) Hematological parameters in ALI mice at 24 h after different treatments. (**A**) WBC count. (**B**) RBC count. (**C**) PLT count. (**D**) Lymph count. (**E**) H&E staining images of heart, liver, spleen, and kidney sections from different groups collected at 7 days post-treatment. Data are presented as mean ± SD (n = 3). Statistical significance was determined using a two-tailed unpaired Student's *t*-test for comparisons between two groups. *$P < 0.05$.
Abbreviation: ns, not significant.

https://doi.org/10.2147/IJN.S608394

staining (Figure 6E). No obvious tissue damage or pathological abnormalities were observed in any treatment group compared to healthy controls, indicating that MΦ@Alum/Toc does not cause significant organ toxicity.

Conclusion

In conclusion, we developed a nanoengineered macrophage platform (MΦ/ICG@Alum/Toc) integrating PACT for real-time theranostics of acute lung injury. By enabling non-invasive tracking of engineered macrophages, PACT revealed rapid pulmonary homing (within 6 h), peak accumulation at 24 h, and subsequent hepatic clearance, with minimal off-target distribution. Aluminum hydroxide-stabilized tocilizumab addressed the challenge of premature exocytosis, enhancing target bioavailability. The platform demonstrated superior anti-inflammatory, antioxidant, and immunomodulatory efficacy compared to free tocilizumab, with excellent biosafety. Overall, this study establishes a clinically translatable strategy combining cell-based delivery with advanced imaging for precision immunotherapy of ALI and other inflammatory diseases.

Abbreviations

ALI, Acute lung injury; ARDS, Acute respiratory distress syndrome; CT, Computed tomography; LUS, Lung ultrasound; MRI, Magnetic resonance imaging; PA, Photoacoustic; PAI, Photoacoustic imaging; PACT, Photoacoustic computed tomography; Toc, Tocilizumab; ICG, Indocyanine green; Alum, Aluminum hydroxide adjuvant; TEM, Transmission electron microscope; UV, Ultraviolet; H&E, Hematoxylin and eosin; LPS, Lipopolysaccharide; LG, Lumogallion; BCA, Bicinchoninic acid assay; CCK-8, Cell Counting Kit-8; 3D, Three-dimensional; DAB, 3,3′-diaminobenzidine; ELISA, Enzyme-linked immunosorbent assay; IHC, Immunohistochemistry; MPO, Myeloperoxidase; MDA, Malondialdehyde; T-SOD, Total superoxide dismutase; WBC, White blood cell; RBC, Red blood cell; PLT, Platelet; Lymph, Lymphocyte.

Data Sharing Statement

The data that support the findings of this study are available from the corresponding author upon reasonable request.

Ethics Approval

All experimental procedures were conducted in strict compliance with institutional guidelines for the care and use of laboratory animals and were approved by the Animal Ethics Committee of Guangzhou Medical University (Approval No. GY2024-287).

Funding

This work was supported by the Major Project of Guangzhou National Laboratory (GZNL2023A03002) and the Key Scientific Research Project of Universities in Guangdong Province (2023KCXTD026).

Disclosure

The authors report no conflicts of interest in this work.

References

1. Gao R, Lin P, Fang Z, et al. Cell-derived biomimetic nanoparticles for the targeted therapy of ALI/ARDS. *Drug Deliv Transl Res*. 2024;14:1432–1457. doi:10.1007/s13346-023-01494-6
2. Long ME, Mallampalli RK, Horowitz JC. Pathogenesis of pneumonia and acute lung injury. *Clin Sci*. 2022;136:747–769. doi:10.1042/CS20210879
3. Zhang J, Guo Y, Mak M, et al. Translational medicine for acute lung injury. *J Transl Med*. 2024;22:25. doi:10.1186/s12967-023-04828-7
4. Matthay MA, Zemans RL, Zimmerman GA, et al. Acute respiratory distress syndrome. *Nat Rev Dis Primers*. 2019;5:18. doi:10.1038/s41572-019-0069-0
5. Cheng P, Li S, Chen H. Macrophages in Lung injury, repair, and fibrosis. *Cells*. 2021;10:436. doi:10.3390/cells10020436
6. Wang Z, Wang Z. The role of macrophages polarization in sepsis-induced acute lung injury. *Front Immunol*. 2023;14:1209438. doi:10.3389/fimmu.2023.1209438
7. Lee JW, Chun W, Lee HJ, et al. The role of macrophages in the development of acute and chronic inflammatory lung diseases. *Cells*. 2021;10. doi:10.3390/cells10040897
8. Liu C, Xiao K, Xie L. Advances in the use of exosomes for the treatment of ALI/ARDS. *Front Immunol*. 2022;13:971189. doi:10.3389/fimmu.2022.971189
9. Lang FM, Lee KM, Teijaro JR, et al. GM-CSF-based treatments in COVID-19: reconciling opposing therapeutic approaches. *Nat Rev Immunol*. 2020;20:507–514. doi:10.1038/s41577-020-0357-7

10. Xing H, Bai X, Pei X, et al. Synergistic anti-oxidative/anti-inflammatory treatment for acute lung injury with selenium based chlorogenic acid nanoparticles through modulating Mapk8ip1/MAPK and Itga2b/PI3k-AKT axis. *J Nanobiotechnology*. 2025;23:37. doi:10.1186/s12951-025-03114-6
11. Wang Q, Wu LL, Zhang Q, et al. In situ photoacoustic visualization of pneumonia induced by MRSA and specific identifying tumor-homing bacteria. *ACS Appl Bio Mater*. 2023;6:4413–4420. doi:10.1021/acsabm.3c00610
12. Zhu B, Xing X, Kim J, et al. Endogenous CO imaging in bacterial pneumonia with a NIR fluorescent probe. *Biomaterials*. 2024;304:122419. doi:10.1016/j.biomaterials.2023.122419
13. Wang X, He S, Cheng P, et al. A dual-locked tandem fluorescent probe for imaging of pyroptosis in cancer chemo-immunotherapy. *Adv Mater*. 2023;35:e2206510. doi:10.1002/adma.202206510
14. Kim J, Lee J, Choi S, et al. 3D multiparametric photoacoustic computed tomography of primary and metastatic tumors in living mice. *ACS Nano*. 2024;18:18176–18190. doi:10.1021/acsnano.3c12551
15. Yang A, Wang Y, Feng Q, et al. Integrating fluorescence and magnetic resonance imaging in biocompatible scaffold for real-time bone repair monitoring and assessment. *Adv Healthc Mater*. 2024;13:e2302687. doi:10.1002/adhm.202302687
16. Ohno Y, Hanamatsu S, Obama Y, et al. Overview of MRI for pulmonary functional imaging. *Br J Radiol*. 2022;95:20201053. doi:10.1259/bjr.20201053
17. Nakamura H, Hirai T, Kurosawa H, et al. Current advances in pulmonary functional imaging. *Respir Investig*. 2024;62:49–65. doi:10.1016/j.resinv.2023.09.004
18. Yu Y, Feng T, Qiu H, et al. Simultaneous photoacoustic and ultrasound imaging: a review. *Ultrasonics*. 2024;139:107277. doi:10.1016/j.ultras.2024.107277
19. Knox HJ, Chan J. Acoustogenic probes: a new frontier in photoacoustic imaging. *Acc Chem Res*. 2018;51:2897–2905. doi:10.1021/acs.accounts.8b00351
20. Wang LV, Hu S. Photoacoustic tomography: in vivo imaging from organelles to organs. *Science*. 2012;335:1458–1462. doi:10.1126/science.1216210
21. Weber J, Beard PC, Bohndiek SE. Contrast agents for molecular photoacoustic imaging. *Nat Methods*. 2016;13:639–650. doi:10.1038/nmeth.3929
22. Reinhardt CJ, Zhou EY, Jorgensen MD, et al. A ratiometric acoustogenic probe for in vivo imaging of endogenous nitric oxide. *J Am Chem Soc*. 2018;140:1011–1018. doi:10.1021/jacs.7b10783
23. Cho S, Kim M, Ahn J, et al. An ultrasensitive and broadband transparent ultrasound transducer for ultrasound and photoacoustic imaging in-vivo. *Nat Commun*. 2024;15:1444. doi:10.1038/s41467-024-45273-4
24. Yao J, Wang LV. Photoacoustic Microscopy. *Laser Photon Rev*. 2013;7:758–778. doi:10.1002/lpor.201200060
25. Kim C, Favazza C, Wang LV. In vivo photoacoustic tomography of chemicals: high-resolution functional and molecular optical imaging at new depths. *Chem Rev*. 2010;110:2756–2782. doi:10.1021/cr900266s
26. Choi W, Park EY, Jeon S, et al. Three-dimensional multistructural quantitative photoacoustic and US imaging of human feet in vivo. *Radiology*. 2022;303:467–473. doi:10.1148/radiol.211029
27. Cao Y, Dumani DS, Hallam KA, et al. Real-time monitoring of NIR-triggered drug release from phase-changeable nanodroplets by photoacoustic/ultrasound imaging. *Photoacoustics*. 2023;30:100474. doi:10.1016/j.pacs.2023.100474
28. Gröhl J, Schellenberg M, Dreher K, et al. Deep learning for biomedical photoacoustic imaging: a review. *Photoacoustics*. 2021;22:100241. doi:10.1016/j.pacs.2021.100241
29. Kajita H, Suzuki Y, Sakuma H, et al. Visualization of lymphatic vessels using photoacoustic imaging. *Keio J Med*. 2021;70:82–92. doi:10.2302/kjm.2020-0010-OA
30. Kempski KM, Wiacek A, Graham M, et al. In vivo photoacoustic imaging of major blood vessels in the pancreas and liver during surgery. *J Biomed Opt*. 2019;24:1–12. doi:10.1117/1.JBO.24.12.121905
31. Fan Z, Wang Y, Li L, et al. Tumor-homing and immune-reprogramming cellular nanovesicles for photoacoustic imaging-guided phototriggered precise chemoimmunotherapy. *ACS Nano*. 2022;16:16177–16190. doi:10.1021/acsnano.2c04983
32. Meng F, Liang C, Ali B, et al. In vivo spatiotemporal characterizing diverse body transportation of optical labeled high immunity aluminium adjuvants with photoacoustic tomography. *Photoacoustics*. 2024;39:100643. doi:10.1016/j.pacs.2024.100643
33. Galanzha EI, Menyaev YA, Yadem AC, et al. In vivo liquid biopsy using cytophone platform for photoacoustic detection of circulating tumor cells in patients with melanoma. *Sci Transl Med*. 2019;11. doi:10.1126/scitranslmed.aat5857
34. Kim J, Park B, Ha J, et al. Multiparametric photoacoustic analysis of human thyroid cancers in vivo. *Cancer Res*. 2021;81:4849–4860. doi:10.1158/0008-5472.CAN-20-3334
35. Park B, Han M, Park J, et al. A photoacoustic finder fully integrated with a solid-state dye laser and transparent ultrasound transducer. *Photoacoustics*. 2021;23:100290. doi:10.1016/j.pacs.2021.100290
36. Fan XP, Huang J, Ren TB, et al. De Novo design of activatable photoacoustic/fluorescent probes for imaging acute lung injury in vivo. *Anal Chem*. 2023;95:1566–1573. doi:10.1021/acs.analchem.2c04642
37. Li Y, Lv J, Liu S, et al. Macrophage corpses for immunoregulation and targeted drug delivery in treatment of collagen-induced arthritis mice. *Biomaterials*. 2025;314:122867. doi:10.1016/j.biomaterials.2024.122867
38. Yue L, Gao C, Li J, et al. Chemotaxis-guided self-propelled macrophage motor for targeted treatment of acute pneumonia. *Adv Mater*. 2023;35:e2211626. doi:10.1002/adma.202211626
39. Xu X, Kwong CHT, Li J, et al. “Zombie” macrophages for targeted drug delivery to treat acute pneumonia. *ACS Appl Mater Interfaces*. 2023;15:29012–29022. doi:10.1021/acsami.3c06025
40. Chao CJ, Zhang E, Zhao Z. Engineering cells for precision drug delivery: new advances, clinical translation, and emerging strategies. *Adv Drug Deliv Rev*. 2023;197:114840. doi:10.1016/j.addr.2023.114840
41. Xu X, Wang Q, Qian X, et al. Spatial-drug-laden protease-activatable M1 macrophage system targets lung metastasis and potentiates antitumor immunity. *ACS Nano*. 2023;17:5354–5372. doi:10.1021/acsnano.2c08834
42. de Almeida MS, Susnik E, Drasler B, et al. Understanding nanoparticle endocytosis to improve targeting strategies in nanomedicine. *Chem Soc Rev*. 2021;50:5397–5434. doi:10.1039/d0cs01127d
43. Myerson JW, Patel PN, Rubey KM, et al. Supramolecular arrangement of protein in nanoparticle structures predicts nanoparticle tropism for neutrophils in acute lung inflammation. *Nature Nanotechnol*. 2022;17:86–97. doi:10.1038/s41565-021-00997-y

44. HogenEsch H, O'Hagan DT, Fox CB. Optimizing the utilization of aluminum adjuvants in vaccines: you might just get what you want. *Npj Vaccines*. 2018;3:51. doi:10.1038/s41541-018-0089-x
45. Nies I, Hidalgo K, Bondy SC, et al. Distinctive cellular response to aluminum based adjuvants. *Environ Toxicol Pharmacol*. 2020;78:103404. doi:10.1016/j.etap.2020.103404
46. Badran G, Angrand L, Masson J-D, et al. Physico-chemical properties of aluminum adjuvants in vaccines: implications for toxicological evaluation. *Vaccine*. 2022;40:4881–4888. doi:10.1016/j.vaccine.2022.06.064
47. Rosas IO, Bräu N, Waters M, et al. Tocilizumab in hospitalized patients with severe Covid-19 pneumonia. *New Engl J Med*. 2021;384:1503–1516. doi:10.1056/NEJMoa2028700
48. Abani O, Abbas A, Abbas F, et al. Tocilizumab in patients admitted to hospital with COVID-19 (RECOVERY): a randomised, controlled, open-label, platform trial. *Lancet*. 2021;397:1637–1645. doi:10.1016/S0140-6736(21)00676-0